energies

MDPI

Article

An Experimental Investigation on the Heat Transfer Characteristics of Pulsating Heat Pipe with Adaptive Structured Channels

Jiangchuan Yu [1], Sihui Hong [1,*], Sasaki Koudai [2], Chaobin Dang [2] and Shuangfeng Wang [3]

[1] Center for Space Technology, School of Physics and Astronomy, Sun Yat-sen University, Zhuhai 519082, China; yujch8@mail2.sysu.edu.cn
[2] Graduate School of Engineering, University of Fukui, 3-9-1 Bunkyo, Fukui-shi 910-8507, Japan; ms220090@u-fukui.ac.jp (S.K.); dangcb@u-fukui.ac.jp (C.D.)
[3] Key Lab of Heat Transfer Enhancement and Energy Conservation of Ministry of Education, School of Chemistry and Chemical Engineering, South China University of Technology, Guangzhou 510640, China; sfwang@scut.edu.cn
* Correspondence: hongsh23@mail.sysu.edu.cn

Abstract: In recent years, the development of electronic chips has focused on achieving high integration and lightweight designs. As a result, pulsating heat pipes (PHPs) have gained widespread use as passive cooling devices due to their exceptional heat transfer capacity. Nevertheless, the erratic pulsations observed in slug flow across multiple channels constitute a significant challenge, hindering the advancement of start-up and heat dissipation capabilities in traditional PHP systems. In this paper, we introduce a flat plate pulsating heat pipe (PHP) featuring adaptive structured channels, denoted as ASCPHP. The aim is to enhance the thermal performance of PHP systems. These adaptive structured channels are specifically engineered to dynamically accommodate volume changes during phase transitions, resulting in the formation of a predictable and controllable two-phase flow. This innovation is pivotal in achieving a breakthrough in the thermal performance of PHPs. We experimentally verified the heat transfer performance of the ASCPHP across a range of heating loads from 10 to 75 W and various orientations spanning 0 to 90 degrees, while maintaining a constant filling ratio (FR) of 40%. In comparison to traditional PHP systems, the ASCPHP design, as proposed in this study, offers the advantage of achieving a lower evaporation temperature and a more uniform temperature distribution across the PHP surface. The thermal resistances are reduced by a maximum of 37.5% when FR is 40%. The experimental results for start-up characteristics, conducted at a heating power of 70 W, demonstrate that the ASCPHP exhibits the quickest start-up response and the lowest start-up temperature among the tested configurations. Furthermore, thanks to the guiding influence of adaptive structured channels on two-phase flow, liquid replenishment in the ASCPHP exhibits minimal dependence on gravity. This means that the ASCPHP can initiate the start-up process promptly, even when placed horizontally.

Keywords: pulsating heat pipe; adaptive structure; thermal resistance; orientation; heat transfer

check for updates

Citation: Yu, J.; Hong, S.; Koudai, S.; Dang, C.; Wang, S. An Experimental Investigation on the Heat Transfer Characteristics of Pulsating Heat Pipe with Adaptive Structured Channels. *Energies* **2023**, *16*, 6988. https://doi.org/10.3390/en16196988

Academic Editor: Dmitry Eskin

Received: 17 August 2023
Revised: 27 September 2023
Accepted: 5 October 2023
Published: 7 October 2023

1. Introduction

In 2020, China's digital economy's core industries contributed 7.8% to the nation's GDP, establishing it as the primary economic sector following agriculture and industry. The rapid growth of the digital economy has introduced a range of challenges, including the imperative to bridge digital divides, enhance cybersecurity, and refine the digital economy's development model [1]. As the microelectronics industry advances towards higher integration, lighter weight, and multifunctionality, the packaging density of electronic chips has experienced a sharp increase. Consequently, the heat flux of electronic chips has increased significantly, profoundly impacting their operational performance. In the temperature range of 70–80 °C, the reliability of a system comprised of electronic components diminishes by 50% for every additional 10 °C in the temperature of individual electronic components. Over recent years, traditional air-cooling and single-phase liquid-cooling technologies have proven inadequate in addressing the demands of high-load heat dissipation and the spatial constraints associated with electronic chips. Moreover, as heat dissipation demands increase, additional power consumption, noise, and leakage issues become more pronounced. The Ministry of Industry and Information Technology has proposed that, between 2021 and 2023, new large-scale data centers and those of higher tiers must decrease their power usage effectiveness (PUE) to below 1.3, with a target of achieving below 1.25 in regions characterized by severe cold and cold climates. In order to further decrease the PUE value of data centers, the thermal management system must opt for more energy-efficient cooling methods [2]. In 1990, Akachi [3,4] proposed a novel heat pipe design, christened the pulsating heat pipe (PHP). The PHP stands out as a highly efficient passive phase-change cooling device, exploiting the working medium to induce a vapor–liquid phase-change between its self-contained hot and cold ends, creating reciprocating vapor–liquid plugs that facilitate heat transfer without the need for supplementary power consumption or extra components. Because pulsating heat pipes lack a sintered core, they can be more readily miniaturized than other heat pipe varieties, making them better suited for cooling chips in space. PHP has emerged as one of the solutions for high-power chip cooling, owing to its remarkable phase-change capability, low thermal resistance, and absence of additional power consumption.

In order to comprehend and enhance the thermal performance of PHP, researchers have conducted a series of investigations. Parameters that impact the heat transfer performance of pulsating heat pipes can be roughly categorized into three groups: (1) Geometric parameters of PHPs: pipe diameter [5–7], section shape [8–11], channel structure [5,12–28], length of evaporating and condensing section [29,30], number of turns [16,31,32], etc. (2) Physical characteristics of working medium filling in PHP [33,34]: surface tension, latent heat, dynamic viscosity, etc. (3) Operation parameters of PHP: liquid filling ratio [35], inclination angle [36], external force [37,38], ambient temperature, etc. This paper primarily investigates the geometric structure of PHPs, and consequently, it primarily presents related research on PHPs' geometric structure.

The microcosmic heat transfer mechanism in PHPs involves liquid film evaporation and condensation. Consequently, researchers aim to reduce the liquid film thickness and enhance thermal performance by altering the shape of the channel cross-section in the PHP. Khandekar and colleagues [8] reported that rectangular channels exhibited an uneven distribution of the liquid film in the channel cross-section compared to circular channels. The working fluid was primarily transported at the channel's edges in a capillary-assisted mode similar to thermosiphon. Their research on the distribution of the liquid film demonstrated that rectangular channels can enhance heat transfer performance. Yang and colleagues [9] experimentally validated Khandekar's conclusion and discovered that rectangular channels altered the flow regime transitions of the liquid within the channel. In their experimental study, Lee and colleagues [10] compared the heat transfer performance and liquid film thickness of rectangular-channeled and circular-channeled PHPs. They discovered that the operational limits of both rectangular and circular-channeled PHPs increased with an increase in the channel's hydraulic diameter. When the hydraulic diameters were equal, a rectangular-channeled PHP exhibited a 70% higher maximum heat flux than a circular-channeled PHP, indicating superior heat transfer capabilities. Hua and colleagues [11] conducted experimental comparisons between rectangular and circular-channeled PHPs, with a primary focus on thermal resistance and temperature difference. The thermal resistance of the rectangular-channeled PHP was found to be only 30–40% of that of the circular-channeled PHP. Under identical experimental conditions, the temperature difference between the evaporation and condensation sections of the rectangular-channeled PHP was lower than that of the circular-channeled PHP. These findings further confirmed the superior heat transfer performance of the rectangular channel.

In addition to examining the shape of the channel cross-section, research on the impact of incorporating additional components to induce directional two-phase flow has also gained popularity. Miyazaki and colleagues [12] conducted experimental investigations on PHPs featuring a check valve structure. The addition of one or more check valve structures in the loop resulted in directional vapor–liquid motion inside the PHP. Their experimental findings demonstrated that the check valve structure can significantly enhance the heat transfer performance of the PHP. Rittidech and colleagues [13] conducted experimental verification, confirming that a check valve effectively guides the two-phase flow within a PHP and enhances its thermal performance. Recently, the Tesla valve structure, initially proposed by Thompson and colleagues [14], has been incorporated into PHP systems to facilitate the creation of orderly two-phase flow through the utilization of pressure differences. The Tesla valve's role is to enhance the circulation of two-phase flow within PHP, ensure the provision of the necessary liquid for heat dissipation, and enhance heat transfer performance. When compared to PHPs lacking a Tesla valve, those equipped with a Tesla valve exhibit a reduction in thermal resistance ranging from 15% to 25%. The exact optimization effect is contingent on the level of heating power. Wan and colleagues [28] incorporated a spring-check valve into the PHP to establish unidirectional circulation of two-phase flow. As a result of this unidirectional flow pattern of the working fluid, the heat transfer capacity of the PHP experienced substantial enhancement. He and colleagues [19] conducted optimizations on the geometric structure of PHPs and introduced a series of conical nozzle structures tailored for three-dimensional PHPs. Experimental findings demonstrated that the thermal resistance of the optimized PHP was reduced by 29.5%, and the introduction of the series of conical nozzle structures notably enhanced unidirectional flow. However, for chip cooling, these check valves and conical nozzle structures are too large to be seamlessly integrated with electronic components. As a result, researchers turned their attention to the internal structure of the channel. Ebrahimi and colleagues [15] introduced the innovative concept of channel interconnection in plate-based PHPs, resulting in a reduction in unidirectional flow resistance and an increase in the overall heat transfer of the fluid. Chien and colleagues [16] introduced asymmetrical PHPs, also referred to as dual-diameter PHPs. In contrast to PHPs with equal diameters, asymmetrical PHPs exhibit reliable operation under diverse placement angles, and their performance improves progressively as the placement angle increases. To assess the heat transfer performance of asymmetric PHPs, Tseng and colleagues [17] conducted experimental comparisons between equal-diameter channels and asymmetric channels. Their findings demonstrated that asymmetric PHPs were easier to initiate and consistently exhibited low thermal resistance at various heating power levels. Additionally, Tseng observed that PHPs with asymmetric channels performed better when oriented vertically. Kwon and colleagues [18] conducted a series of experiments to confirm the finding that asymmetric PHPs exhibit lower thermal resistance. Additionally, Jang and colleagues [5] determined the optimal aspect ratio of the channel and the asymmetric proportion of asymmetrical PHPs through experiments at heating power levels of 6 W, 12 W, and 18 W. Kang and colleagues [27] developed an innovative PHP incorporating separating walls within the channel. Using computational fluid dynamics (CFD) to evaluate the heat transfer performance of the new PHP, they determined that, in comparison to the classical PHP without separating walls, the new PHP exhibited a 14% enhancement in thermal performance. Krambeck and colleagues [39] modified the evaporation channels of the PHP by incorporating ultra-sharp lateral grooves. This alteration resulted in a 12% enhancement in thermal performance.

Previous research indicates that the asymmetric design in the channel's geometric structure of PHPs has a significant impact on facilitating unidirectional circulation of two-phase flow and significantly enhancing heat transfer performance. Miner and colleagues [20,21] conducted experimental investigations to explore the impact of expanding the cross-section on the heat transfer performance of microchannel flow boiling. Their findings revealed that expanding the cross-section in the flow direction of the microchannel led to an improvement in flow boiling heat transfer performance by stabilizing the thin liquid film beneath elongated bubbles. The heat transfer performance of the expanded microchannel was 1.5 times greater than that of the straight microchannel, and the frictional pressure drop was reduced by 2/3. Additionally, we recently conducted visualization experiments to confirm the beneficial impact of expanded microchannels on enhancing flow boiling behaviors [22–25]. The results suggested that the use of expanding microchannels allows for the maintenance of stable flow boiling, even under conditions of low inlet inertia and two-phase flow. Furthermore, the rapid and directional vapor removal in expanding microchannels results in consistent thin liquid film evaporation, virtually suppressing flow reversal under extreme operating conditions.

Just as the impact of expanding microchannels on boiling behavior was explored, the influence of contracting microchannels on two-phase flow condensation was also examined. Lee and colleagues [26] conducted computational fluid dynamics (CFD) simulations to assess the condensing performance of the contracting minichannel. The simulations demonstrated that the contracting minichannel played a substantial role in enhancing the flow condensing process. Owing to the pronounced velocity gradient, vapor acceleration within the contracting minichannel intensified the interfacial shear stress, resulting in a substantial reduction in liquid film thickness along the contracting minichannel and a significant enhancement in heat transfer performance. In comparison to the straight minichannel, the contracting minichannel exhibited a 15% reduction in average liquid film thickness and an approximately 1.4-fold improvement in heat transfer performance.

To enhance the heat transfer performance of PHP for high-power chip cooling, this paper introduces a novel PHP design with adaptive structured channels (ASCPHP). The distinctive feature of these adaptive structured channels lies in their ability to generate a net interfacial force via the asymmetric vapor slug interface within the channel. This net interfacial force acts as auxiliary driving power, resulting in a stable and directional circulating pulsation of the vapor–liquid two-phase flow within the PHP. More precisely, the cross-section of the adaptive structure channel expands throughout the evaporation section and contracts within the condensation section, aligning with the volume changes during the respective phase-change processes of evaporation and condensation. Using experimental methods, this study examined the thermal performance of the ASCPHP, encompassing aspects such as thermal resistances, start-up characteristics, and temperature variations, across various operating conditions (liquid filling ratio, orientation, and heating load). In order to validate the heat transfer enhancement of the ASCPHP, this study compared it with a conventional PHP featuring equal-diameter channels (ECPHP) and asymmetrical channels (ACPHP). The experimental investigation into the thermal performance of the newly proposed ASCPHP is anticipated to offer valuable insights for the future design of thermal management devices for high-flux chip cooling.

2. Experimental Apparatus

2.1. Prototype Design

To describe the oscillation behavior of vapor–liquid slug flow, this study treats the adjacent liquid slug within the tube as a mass point, while the expansion or contraction of the vapor slug between the liquid slugs is modeled as a spring. The oscillatory motion is characterized by a second-order differential equation with forced damping oscillation, and the modulus of resilience is influenced by both the volume and physical properties of the vapor [40].

$$\frac{\mathrm{d}^2x}{\mathrm{d}t^2} + \frac{\alpha}{m}\frac{\mathrm{d}x}{\mathrm{d}t} + \omega_0^2 x = \frac{F}{m}\cos\omega t \tag{1}$$

where α is the total pressure drop caused by frictional losses, and m represents the total mass of gas and liquid within the PHP, denoted as $(L_l\rho_l + L_v\rho_v)$. ω_0 and ω represent the undamped natural frequency and oscillation frequency, respectively.

Considering the friction resistance F_f of the two-phase flow and the deformation resistance ΔP_v of the compressible vapor slug during the pulsating motion of the slug-flow in the PHP, a "spring-mass-damping" pulsation dynamics model is thereby established [40], shown as Equation (2):

$$(L_l\rho_l + L_v\rho_v)\frac{\mathrm{d}^2x}{\mathrm{d}t^2} - \left(\frac{\mathrm{d}P}{\mathrm{d}z}\right)_{tp} + \frac{\rho_v RT}{L_v}x = \left(\frac{h_{lv}\rho_v}{T}\right)\left(\frac{\Delta T_{max} - \Delta T_{min}}{2}\right)[1+\cos(\omega t)] \quad (2)$$

where $-\left(\frac{\mathrm{d}P}{\mathrm{d}z}\right)_{tp}$ is the two-phase flow pressure drop of the slug flow given by the separated two-phase flow model, which contains the frictional pressure drop, acceleration pressure drop, and gravitational pressure drop [41], e.g.,

$$-\left(\frac{\mathrm{d}P}{\mathrm{d}z}\right)_{tp} = \frac{\frac{\mathrm{d}F_v + \mathrm{d}F_l}{A\mathrm{d}z} + G^2\frac{d}{dx}\left[\frac{x^2}{\beta\rho_v} + \frac{1-x^2}{(1-\beta)\rho_l}\right] + [\beta\rho_v + (1-\beta)\rho_l]gsin\theta}{1 - Ma^2} \quad (3)$$

where Ma is the Mach number [41], given as:

$$Ma^2 = -G^2\left\{\frac{x^2}{\alpha}\left(\frac{\partial v_v}{\partial p}\right) + \left(\frac{\partial \beta}{\partial p}\right)_x\left[\frac{(1-x^2)v_l}{(1-\alpha)^2} - \frac{x^2 v_v}{\alpha^2}\right]\right\} \quad (4)$$

where v_l and v_v are the specific volume of vapor and liquid phase, respectively; L_l and L_v are the length of vapor and liquid slug, respectively; and x and α are the local vapor quality and void fraction, respectively.

In the adaptive structured channel proposed in this work, the cross-section of channel varies along the flow direction. Vapor slug in the channel is subjected to additional pressure P_c from the vapor–liquid interface, shown as Figure 1a. The $P_{c,net}$ induced by the asymmetric interface is given by Equation (5).

$$P_{c,net} = \frac{2\sigma cos\theta}{R_1} - \frac{2\sigma cos\theta}{R_2} \quad (5)$$

where σ is the coefficient of surface tension, and R_1 and R_2 are the radiuses of the curvature at the upstream and downstream interface of the vapor slug. θ is the static contact angle of the working fluid on the channel surface. In the evaporation section, as the curvature radius R gradually increases along the flow direction, the net additional pressure directs to the forward flow direction.

When liquid evaporates in the evaporation section, the heat flux causes the evaporation mass flux. This results in a momentum change between the two vapor–liquid phases caused by mass transfer during the conversion from liquid to vapor [24], shown as Figure 1a. The evaporative momentum force per unit length can be given by Equation (6).

$$F'_{M,net} = \left(\frac{q}{h_{fg}}\right)^2\frac{D_2 - D_1}{\rho_v} \quad (6)$$

where D is the characteristic dimension, the subscripts 1 and 2 refer to the upstream and downstream interfaces of the vapor slug, $\frac{q}{h_{fg}}$ is the evaporation mass flux, and ρ_v is the vapor density. The total evaporative momentum force F_M at the liquid interface can be obtained by integrating l at the vapor–liquid interface. In the expanding section, the liquid interface length increases gradually along the flow direction. Therefore, the resultant direction of the vapor slug evaporation momentum force is the same as the flow direction, which is conducive to the flow of the two-phase flow.

Both of these forces acting on the vapor–liquid interface in the evaporation section have a beneficial impact on vapor removal. The expanding section effectively enhances the pulsation of the two-phase flow and boosts heat transfer within the evaporation section. Similarly, the contracting section within the condensing section also enhances the two-phase flow. As depicted in Figure 1b, the contracting cross-section accelerates the vapor–liquid slug, leading to a reduction in liquid film thickness and an enhancement in heat transfer performance [26]. Consequently, it is evident that applying the expanding and contracting sections to the PHP can enhance the flow of the vapor–liquid slug and improve the heat transfer performance of the PHP. The optimized performance of the ASCPHP was further confirmed through a series of experiments detailed below.

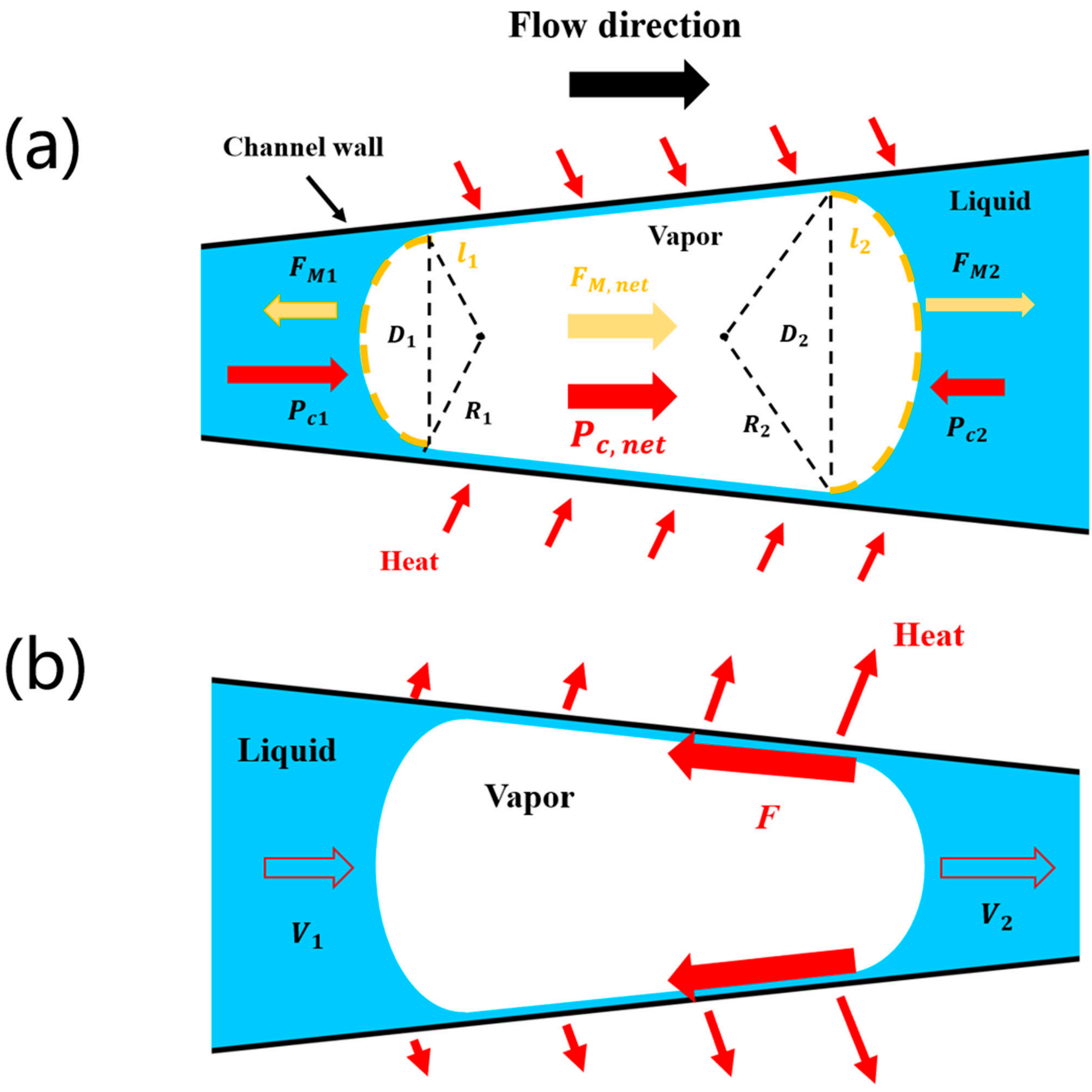

Figure 1. Schematic diagram of working principles of the expanding section and contracting section. (**a**) is a bubble analysis chart for the expanding channel; (**b**) is a bubble analysis chart for the contracting channel.

This study compares three types of PHPs with different designs: a PHP with equal-diameter channels (ECPHP), a PHP with asymmetric-diameter channels (ACPHP), and a PHP with adaptive structured channels (ASCPHP). Figure 2 illustrates the schematic diagrams of these three PHP types. In this study, the maximum and minimum hydraulic diameters are 2 mm and 1 mm, respectively. The hydraulic diameter of the channel between the expanding section and the contracting section remains constant. The parameters of three PHPs with distinct structures are presented in Table 1. The quantity and length of the channels are identical, and the total volume of the PHPs is nearly equivalent. Specifically, the total volumes of the ECPHP, ACPHP, and ASCPHP are 3902.70 mm^3, 3902.70 mm^3, and 3901.68 mm^3, respectively. The channel volume of the ASCPHP differs by only 0.02 mm^3 compared to the other two PHPs, which represents a mere 0.0005% difference relative to the total volume. The influence of the volume difference of the filling medium on the experimental results can be avoided.

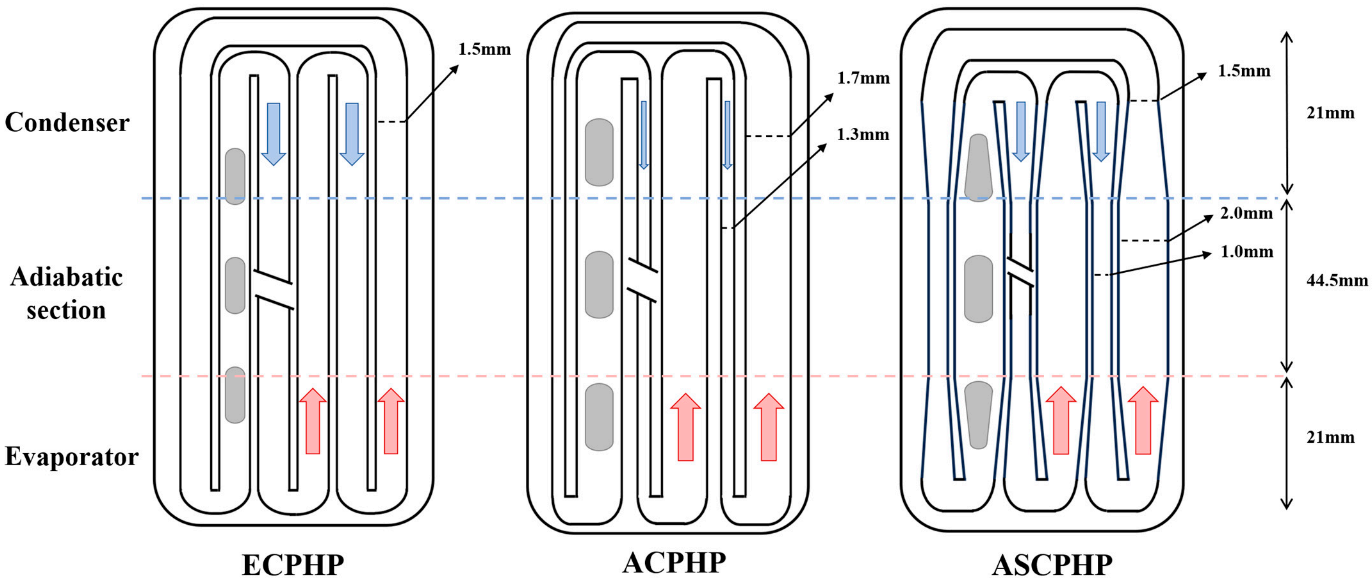

Figure 2. Design diagrams of equal-diameter channel (ECPHP), asymmetric-diameter channel (ACPHP), and adaptive structured channel (ASCPHP) PHPs. The gray shapes represent bubbles, while the blue arrows indicate the direction of condensation flow, and the red arrows denote the direction of evaporation flow.

Table 1. Structure parameters of pulsating heat pipes.

Parameters	PHP Types		
	ECPHP	ACPHP	ASCPHP
D_{max} (mm)	1.5	1.7	2.0
D_{min} (mm)		1.3	1.0
Channel depth (mm)	1.5	1.5	1.5
Total length (mm)	86.5	86.5	86.5
Expansion angle	0°	0°	1.36°
Number of channels	18	18	18

2.2. Test Loop and Operating Conditions

The testing loop is shown as Figure 3a,b, including the PHP test section, data acquisition system, and vacuum filling system.

PHP test loop. The plate PHP consisted of a base plate and a cover plate, as depicted in Figure 3a. The base plate, constructed from 316L stainless steel, featured 18 parallel channels milled end to end. For ease of observing the phenomenon, the cover plate was made from acrylic. There were dedicated grooves on the stainless steel plate for accommodating O-rings, employing axial sealing. After applying vacuum grease to the O-rings and placing them in the grooves, a PC board was positioned on top of the steel plate, followed by compression sealing with a stainless steel frame. Subsequently, vacuum was applied, and the internal pressure changes were monitored. After 5 h, the internal pressure within the experimental setup exhibited a change of less than 1 kPa. Furthermore, to prevent the generated vapor from escaping into adjacent channels through the gap between the channel's top and the cover plate, each channel was sealed using K-6311 UV curable adhesive. In the PHP's evaporation section, a copper block with an inserted heating rod (maximum power: 100 W, resistance: 100 Ω) served as the heat source. The heat load was provided by a DC power supply (SS-L1503SPD). In the condensation section of the PHP, a liquid-cooling loop and a plate heat exchanger were employed to cool down the superheated vapor. The liquid-cooling loop was regulated by a thermostatic water bath (BLKII-1YF-R). The areas of the evaporation and condensation sections were 84×15 mm^2 and 84×48 mm^2, respectively, as depicted in Figure 3d. In order to minimize heat loss to the surroundings, the PHP was positioned inside an insulation box constructed from epoxy resin, featuring an 11 mm thickness. Additionally, each PHP was fitted with a steel pipe, having an outer diameter of 6 mm and an inner diameter of 2 mm, which functioned as the filling pipe. Figure 4 depicts various orientations of the PHPs, with alterations in orientation achieved by adjusting the support bracket shown in Figure 4b.

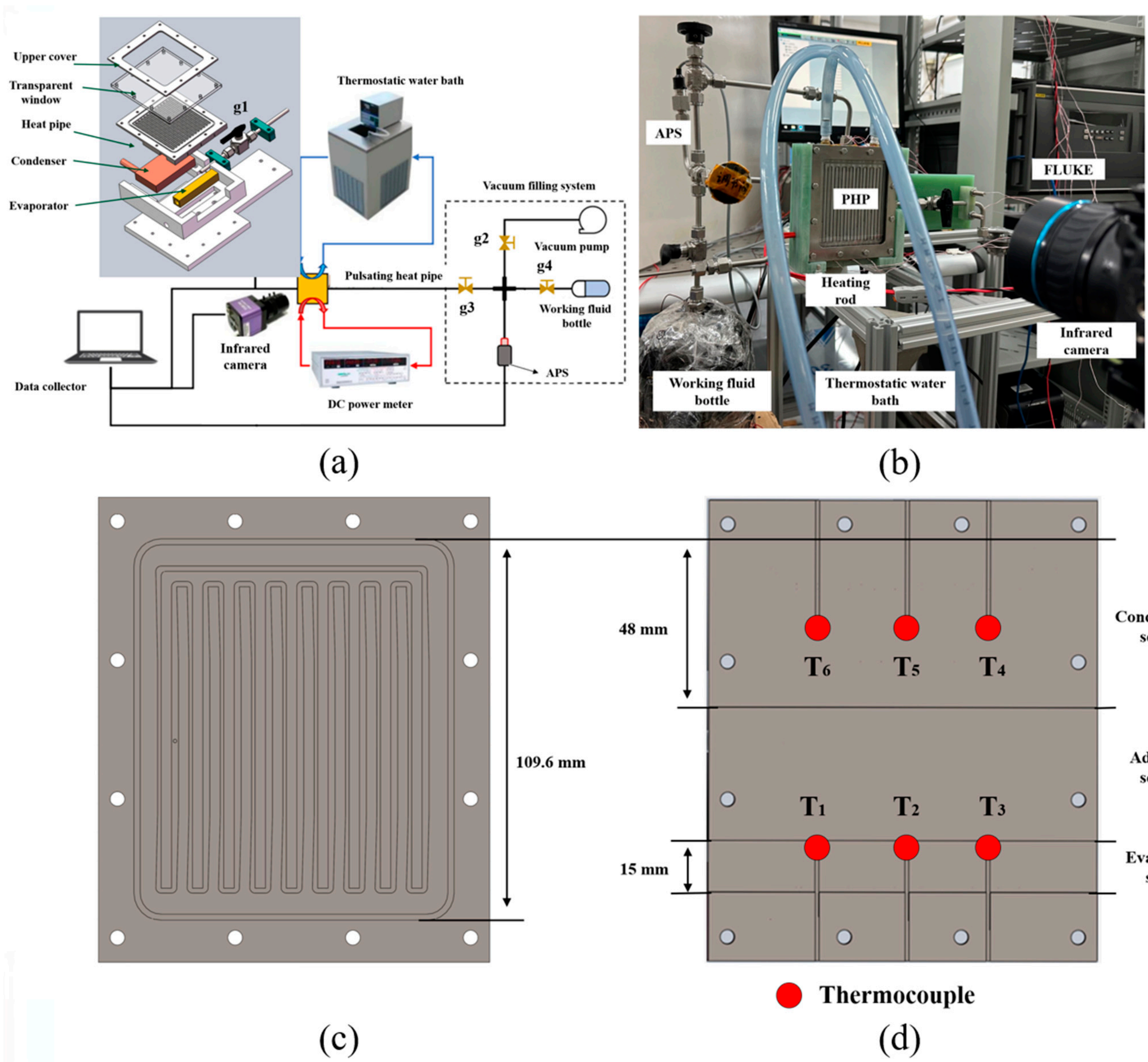

Figure 3. (**a**) Schematic diagram of test loop, (**b**) image of experimental apparatus, (**c**) schematic diagram of PHP, and (**d**) temperature distribution of thermocouple.

Data acquisition system. The surface temperatures of the PHP were measured using T-type thermocouples (OMEGA 5TC-TT-T-30-72, Norwalk, CT, USA) and recorded with a FLUKE data collector (2680A-PAI, Walnut Creek, CA, USA). The distribution of temperature measuring points is depicted in Figure 3d. Prior to the experiments, the thermocouples underwent calibration. Due to considerations regarding the airtightness of the apparatus and the potential interference of excess space on fluid oscillations within the channels, real-time pressure monitoring was not feasible during the experimental procedure. An infrared camera (FLIR A655sc, Salt Lake City, UT, USA) was employed to capture the temperature distribution on the PHP surface. Furthermore, high-speed cameras (FASTCAM Mini AX200, Photron, Japan) were used to record the visualization results of the experiment.

Vacuum and filling system. As depicted in Figure 3a,b, the vacuum and filling system comprised a rotary vane vacuum pump, a well-insulated stainless steel tank (with a volume of 0.35 L), a four-way needle valve, an absolute pressure sensor (with a range of 0–2 MPa), and two T-type thermocouples. The working fluid employed in this study was FC-72 (3M™ Fluorinert™ Electronic Liquid, Deep River, CT, USA) and the tank's wall was equipped with two heating belts to control the working liquid's saturation point. To minimize the impact of non-condensable gas on the PHP's heat transfer characteristics, the working fluid underwent degassing in the container before being filled into the PHP. Initially, the FC-72 within the storage container was subjected to a temperature increase, and changes in vessel pressure were observed while using a vacuum pump for gas evacuation. The degassing process was carried out in accordance with the thermophysical properties of saturated FC-72. Subsequently, we conducted pressure verifications within the storage tank at saturation temperatures of 30 °C, 40 °C, and 60 °C after the aeration process, ensuring the absence of non-condensable gases within the working fluid. The experiment ensured that the initial pressure for all three different PHPs remained consistent throughout the filling process. Prior to each liquid charging, the storage tank was heated to 40 °C, at which point the initial pressure of the PHP was equivalent to the saturation pressure of FC-72 at 40 °C, which is 54 kPa. The FR of the liquid in the PHP was adjusted using a static weighing method with a precision balance (CP4202S, China).

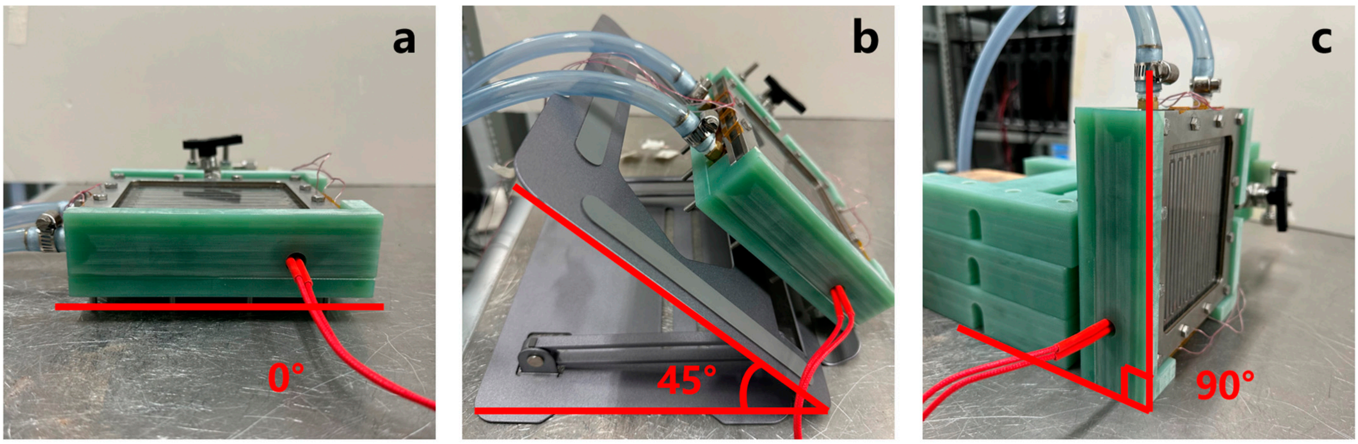

Figure 4. Orientation diagram of PHP, where (**a**–**c**) represent 0°, 45°, and 90°, respectively.

2.3. Data Processing

The thermal resistance was determined according to Equation (7). Here, T_e and T_c are the temperature of the evaporation section and condensation section, respectively. Q is the heat load of the heating rod.

$$R = \frac{T_e - T_c}{Q} \tag{7}$$

The experiment errors mainly resulted from the measurement of the thermocouples and the accuracy of the voltage and current supplied by the DC power. The Class B uncertainty of the T-type thermocouple was 0.2 K. The minimum temperature of the evaporation was 20 °C. The accuracies of the voltage and current of the DC power supply were ±(0.02% of U_{max} + 5 mV) mV and ±(0.1% of I_{max} + 0.1% of FS) mA. The maximum voltage and current were 86.6 V and 0.866 A. Based on the standard error analysis method with Equations (8)–(10), the maximum uncertainty of thermal resistance R was 1.58%.

$$\frac{\delta Q}{Q} = \pm\sqrt{\left(\frac{\delta U}{U}\right)^2 + \left(\frac{\delta I}{I}\right)^2} = \pm\sqrt{1.49984 \times 10^{-4}} = \pm 0.01225 \tag{8}$$

$$\frac{\delta T}{T} = \pm\frac{\sqrt{\frac{\sum_{i=1}^{n}\left(T_i - \overline{T}\right)^2}{n(n-1)} + 0.2^2}}{T_{min}} = \pm\frac{\sqrt{6.2115 \times 10^{-5} + 0.2^2}}{20} = \pm 0.01 \tag{9}$$

$$\frac{\delta R}{R} = \pm\sqrt{\left(\frac{\delta T}{T}\right)^2 + \left(\frac{\delta Q}{Q}\right)^2} = \sqrt{0.01^2 + 1.49984 \times 10^{-4}} = 1.58\% \tag{10}$$

The formula for calculating the FR is given by Equation (11),

$$FR = \frac{M_2 - M_1}{\rho V} \tag{11}$$

Here, M_1 and M_2 correspond to the PHP's inherent mass and the mass of the PHP after filling, respectively. ρV represents the mass of working fluid required to completely charge the PHP. The uncertainties for M_1 and M_2 are calculated using Equations (12) and (13).

$$\frac{\delta M_1}{M_1} = \sqrt{\left(\frac{0.01}{M_{1-max}}\right)^2} = \sqrt{\left(\frac{0.01}{3227.31}\right)^2} = 0.00031\% \tag{12}$$

$$\frac{\delta M_2}{M_2} = \sqrt{\left(\frac{0.01}{M_{2-max}}\right)^2} = \sqrt{\left(\frac{0.01}{3231.23}\right)^2} = 0.00031\% \tag{13}$$

The uncertainty in working fluid density is assumed to be 0. The working fluid volume is determined using Equation (14), and the uncertainty in volume is calculated using Equation (15), as follows:

$$V = H \times W \times L \tag{14}$$

$$\frac{\delta V}{V} = \sqrt{\left(\frac{\delta H}{H}\right)^2 + \left(\frac{\delta W}{W}\right)^2 + \left(\frac{\delta L}{L}\right)^2} = \sqrt{\left(\frac{0.01}{1.50}\right)^2 + \left(\frac{0.01}{2.0}\right)^2 + \left(\frac{0.01}{1734.51}\right)^2} = 0.83\% \tag{15}$$

Subsequently, the uncertainty in the FR can be determined using the following formula:

$$\frac{\delta FR}{FR} = \sqrt{\left(\frac{\delta M_1}{M_1}\right)^2 + \left(\frac{\delta M_2}{M_2}\right)^2 + \left(\frac{\delta \rho}{\rho}\right)^2 + \left(\frac{\delta V}{V}\right)^2} = 0.83\% \tag{16}$$

3. Results and Discussion

3.1. Temperature Variations under Different Heat Loads

Temperature variation curves for three different PHPs with identical liquid filling ratios were compared. These curves depict temperature changes over time under different heat loads and are illustrated in Figures 5 and 6. These figures correspond to a FR of 40%. The heat load varied from 10 to 75 W. To maintain consistency, the temperature of the condensing section was controlled at 10 ± 1 °C, and the initial temperature of the evaporation section was set to 20 °C.

Figure 5 displays infrared photos depicting the temperature distribution on the different types of PHPs operating at 75 W heating power with a liquid FR of 40%. As evident from the infrared photos, the ASCPHP exhibited lower temperatures at corresponding positions, indicating superior heat transfer performance.

Figure 6 demonstrates that at a 40% liquid FR, the temperatures in the evaporation section of the PHP with adaptive structured channels remained consistently lower than those of the ECPHP and ACPHP when subjected to the same heating power. Furthermore, its temperature reached thermal equilibrium more rapidly. Under low-power heating conditions, the ECPHP required an average of 554 s to reach thermal equilibrium at various power levels, while the ACPHP and ASCPHP necessitated 396 s and 352 s, respectively. The ASCPHP consistently achieved thermal equilibrium more rapidly, with the equilibrium temperature being lower than that of the ECPHP and ACPHP. For instance, under a heating power of Q = 35 W, when thermal equilibrium was achieved for the ECPHP, the temperature T_3 reached approximately 50 °C, whereas for the ACPHP and ASCPHP, it was only 45 °C and 39 °C, respectively, representing reductions of 10% and 22%. As the heating power increased, the superior thermal performance of the ASCPHP became increasingly evident. At Q = 75 W, the temperatures in the evaporation section of the ECPHP and ACPHP reached 80 °C and 70 °C, respectively, whereas the ASCPHP maintained a temperature of only 60 °C. In comparison to the ECPHP, the temperatures in the evaporation section of the ACPHP and ASCPHP were reduced by 12.5% and 25%, respectively.

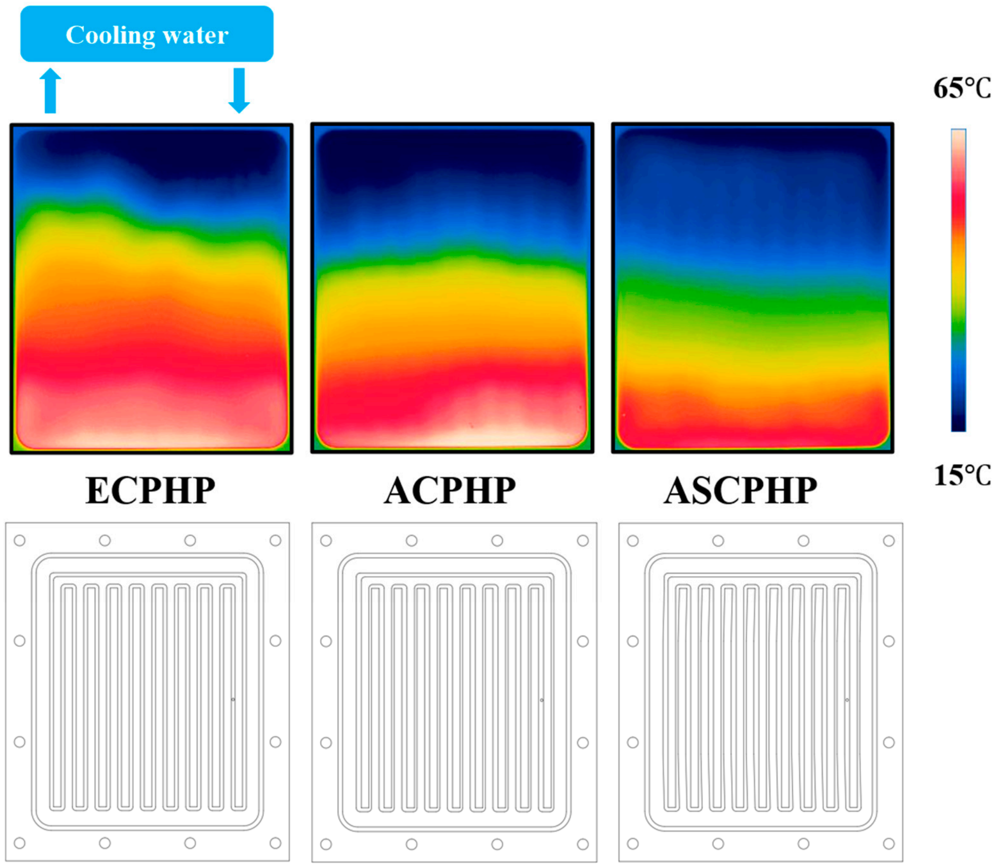

Figure 5. Infrared photo of the temperature distribution the three types of PHPs with FR of 40% (Q = 75 W).

It is important to note that temperature drops in the evaporation section were observed in all three types of PHPs (highlighted by red and yellow circles in the figures). This temperature drop can be attributed to two mechanisms. At lower heating powers, the temperature drops initially occurred in the ECPHP and ACPHP, signifying the commencement of the PHP's operation. Considering the visualization observations, it becomes apparent that vapor and liquid columns in only some channels exhibited small-amplitude oscillations before reaching the temperatures marked by the red circles (ECPHP: 49 °C, ACPHP: 48 °C). Afterward, vapor–liquid slugs in most channels began to oscillate, signifying the full activation of the PHPs. The enhanced oscillatory behavior of the two-phase flow in the PHPs contributed to improved heat transfer performance and, as a result, a decrease in temperature in the evaporation section. The oscillation of vapor–liquid slugs commenced in each channel from the outset of heating and intensified with increasing heat load. Consequently, the ASCPHP exhibited no substantial temperature drop. A more comprehensive comparison of the PHPs' startup characteristics is provided in Section 3.2. At high heating power levels, temperature drops were observed in both the ACPHP and ASCPHP. This improvement can be attributed to the development of the flow pattern, transitioning from slug flow in the PHPs, which enhanced heat transfer performance. Furthermore, as the flow pattern developed in localized channels, the frictional pressure resistance of the two-phase flow in the PHPs decreased. As a result, two-phase flow oscillations in the PHPs intensified, leading to further improvements in heat transfer performance and subsequent temperature reductions.

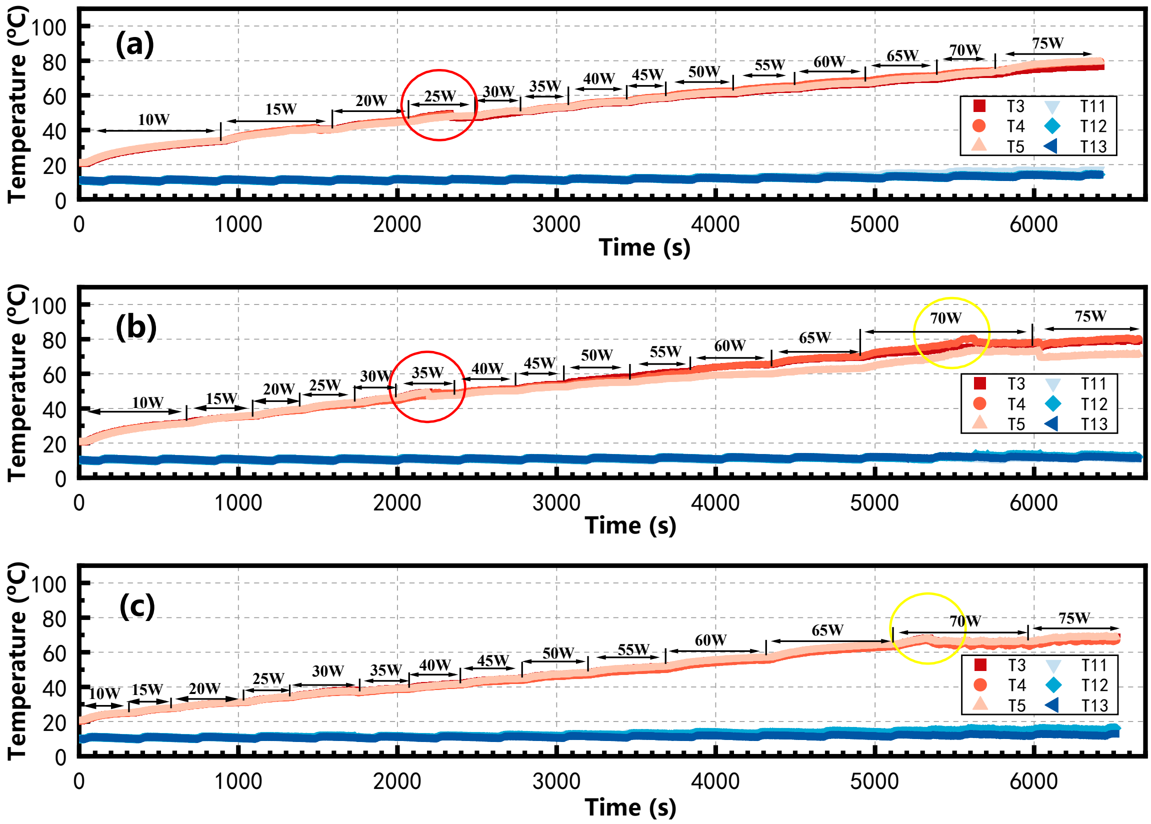

Figure 6. Thermal performances of (**a**) ECPHP, (**b**) ACPHP, and (**c**) ASCPHP under various heat loads (FR = 40%).

3.2. Start-Up Characteristics under High Heat Load

The start-up response of a PHP is critical for efficiently dissipating heat from high-power chips. A slow start-up response can lead to overheating, burnout, or even pose the risk of an explosion for the heat source. Therefore, it is imperative to investigate the start-up characteristics of PHPs, particularly under high heating power conditions. As described in this section, we conducted a comparative experimental study to analyze the start-up time and start-up temperature of three different PHPs under high-power scenarios. The heating power was set at 70 W, with the cooling water inlet temperature at 10 °C, and the initial temperature of the evaporation section at 20 °C.

In Figure 7, the black, red, and blue curves correspond to the ECPHP, ACPHP, and ASCPHP, respectively. At a liquid FR of 40%, as depicted in Figure 7, both the ACPHP and ASCPHP exhibited noticeable temperature overheating followed by a subsequent decrease during startup. This phenomenon is termed the full startup of the PHP, indicating the occurrence of vapor–liquid slug oscillation in all channels. The ECPHP exhibited no significant temperature overshoot, gradually reaching thermal equilibrium at t = 1507 s, with the temperature stabilizing at approximately 74 °C. The ACPHP achieved full startup at 1654 s, maintaining a wall temperature of about 71 °C. The ASCPHP reached full startup in 1249 s, and thereafter, the wall temperature periodically fluctuated around 65 °C once it reached a thermal equilibrium state. The periodic temperature fluctuations observed in ASCPHP, which were a consequence of the pressure difference generated due to overheating, suggest that vapor–liquid slugs within ASCPHP had established a stable and unidirectional cycle within the PHP under high heating power conditions. Summarizing the findings in Figure 7, it is apparent that when subjected to high power, the ASCPHP with an FR of 40% outperformed the other two types of PHPs in startup characteristics, displaying both lower startup temperatures and shorter response times.

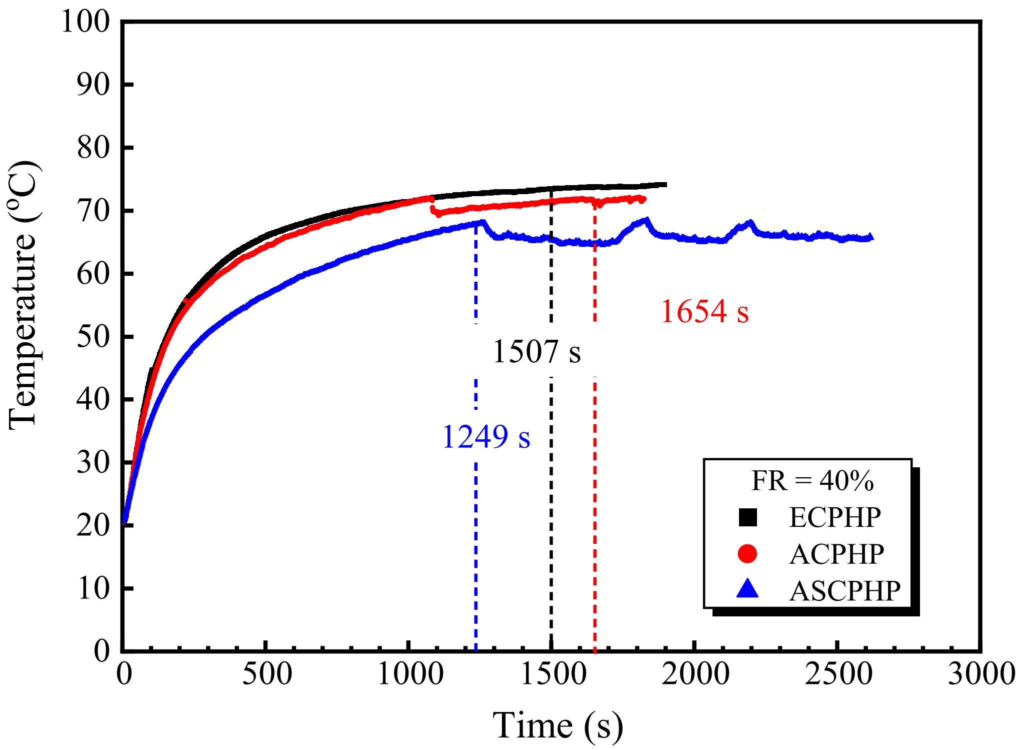

Figure 7. Comparison of start-up characteristics including the start-up temperature and responsive time of the three types of PHPs under Q = 70 W.

3.3. Thermal Resistance

Thermal resistance represents the resistance encountered in the heat transfer path. In the context of PHP, it is commonly used to evaluate the heat transport capability of the working medium between the evaporation and condensation sections. A lower thermal resistance signifies a more effective heat transport capacity within the PHP, leading to a smaller temperature difference between the hot and cold ends.

Figure 8 compares the thermal resistances of three PHPs at a 40% fill ratio condition. As depicted in Figure 8, with increasing heating power, the thermal resistances of all three PHPs gradually decreased until reaching a plateau. The ASCPHP consistently exhibited the lowest thermal resistance, with a minimum of 0.69 °C/W achieved at 55 W. At lower heating powers, the ASCPHP demonstrated the most significant reduction in thermal resistance, with a decrease of up to 37.5% compared to the other two PHPs. However, as heating power increased, the mitigating effect of the ASCPHP on thermal resistance diminished gradually. It is worth noting that the ACPHP and ECPHP exhibited similar thermal resistances throughout, suggesting that under low fill ratio conditions, the asymmetric structure does not significantly optimize two-phase flow and heat transfer processes. Overall, under all operating conditions, the ACPHP and ASCPHP outperformed ECPHP in terms of heat transfer performance. Particularly under low fill ratio conditions, the ASCPHP demonstrated outstanding performance.

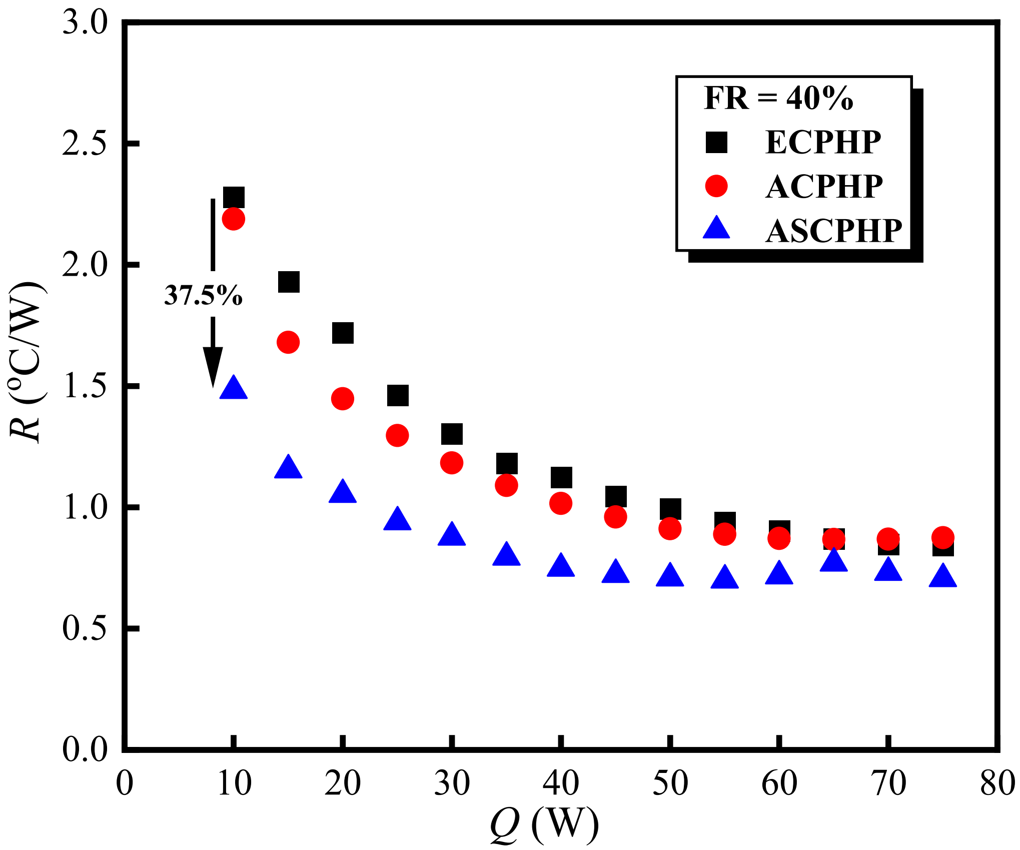

Figure 8. Thermal resistances of three types of PHPs with FR of 40%.

3.4. Effect of Orientation

Because traditional PHPs lack a capillary wick, their thermal performance is significantly affected by gravity. To validate the superior thermal performance of the ASCPHP, experiments were conducted at different orientations, including 0°, 45°, and 90°.

ECPHP, when placed horizontally, failed to initiate. As depicted in Figures 9a and 10a, the temperature curve of ECPHP continued to rise with a heating power of 40 W, without exhibiting a stabilizing trend, potentially leading to overheating if heating were to persist. When the orientation was adjusted to 45°, the ECPHP's thermal performance significantly improved. However, as the thermal load reached 60 W, the ECPHP's thermal resistance started to increase, indicating a deterioration in thermal performance. At an orientation of 90°, the ECPHP's thermal performance was enhanced by 21.8% compared to the 45° orientation. The experimental results for the ECPHP align with the conclusions drawn in previous studies [36]. Due to the asymmetric structure and adaptive design of the channels, the frictional pressure drop within the channels is reduced. Consequently, both the ACPHP and ASCPHP operate effectively when placed horizontally. For the ACPHP, as shown in Figure 10b, thermal resistance significantly decreased when the orientation exceeded 45°. With an increase in heating power, the influence of orientation on ACPHP's thermal resistance gradually diminished. For the ASCPHP, as illustrated in Figure 10c, thermal resistance remained relatively low when placed horizontally compared to the other two PHP types, indicating superior heat transfer performance. Furthermore, when the orientation changed from 0° to 45°, the ASCPHP exhibited a smaller improvement in thermal resistance compared to the other two PHP types, suggesting a lower dependence on gravity. When placed entirely vertically, the ASCPHP's heat transfer performance was further enhanced due to steam acceleration and gravity-induced thin liquid films, resulting in the lowest thermal resistance.

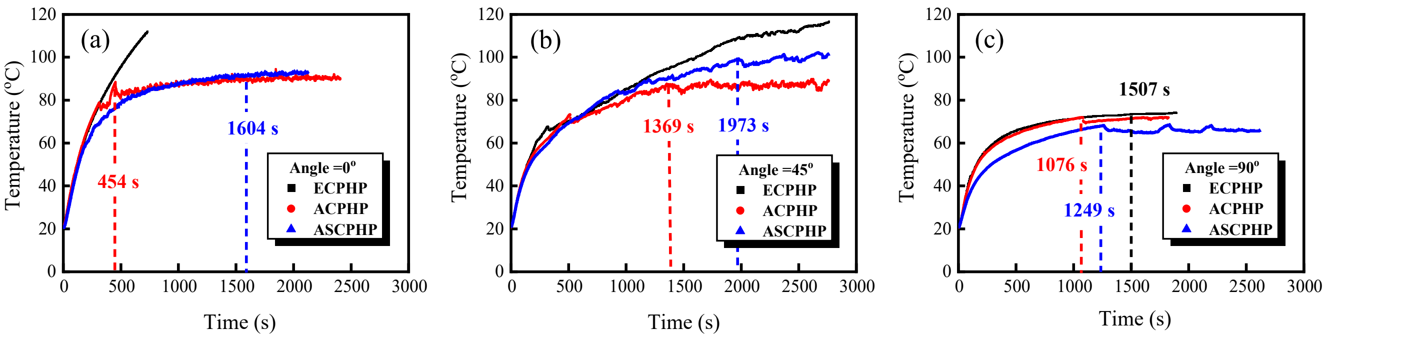

Figure 9. Start-up characteristics of three types of PHPs when placed at 0°, 45°, and 90° (Q = 70 W). (**a**) Temperature Curves for Three PHP Configurations at a 0° Inclination; (**b**) Temperature Curves for Three PHP Configurations at a 45° Inclination; (**c**) Temperature Curves for Three PHP Configurations at a 90° Inclination.

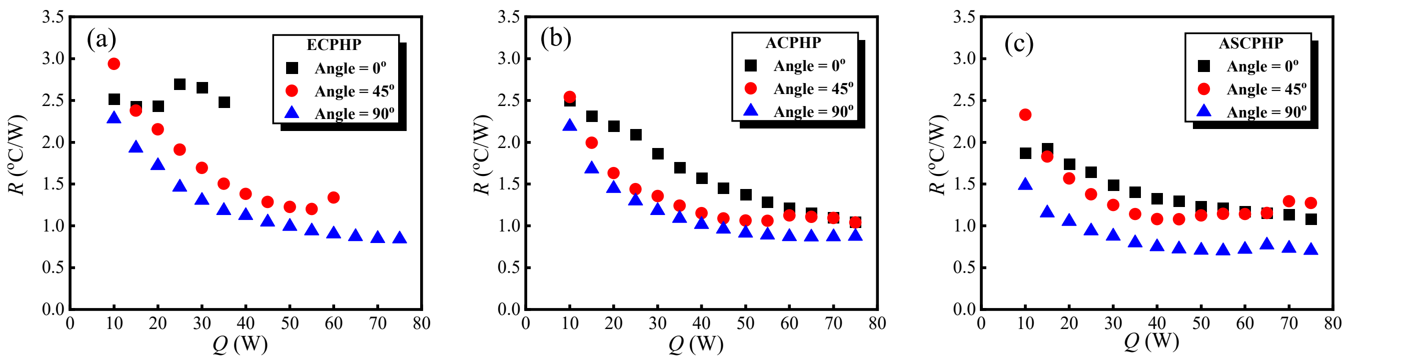

Figure 10. Thermal resistances of the three PHPs when placed at 0°, 45°, and 90°. (**a**) Temperature Curves for Three PHP Configurations at a 0° Inclination; (**b**) Temperature Curves for Three PHP Configurations at a 45° Inclination; (**c**) Temperature Curves for Three PHP Configurations at a 90° Inclination.

4. Conclusions

In this research, we introduced a novel prototype of a PHP with adaptive structured channels. We substantiated the superior thermal performance of the ASCPHP through a comprehensive series of comparative experiments, encompassing its operational characteristics, start-up response, and thermal resistance. We used conventional PHPs with equal-diameter channels and asymmetric-structured channels for comparative purposes. Additionally, we conducted an investigation into the influence of orientation on thermal resistance and start-up response.

Some conclusions can be drawn as follows:

1. The ASCPHP reached thermal equilibrium more quickly than the other types, and when the FR was set to 40%, it maintained the lowest temperature. This was due to the more uniform temperature distribution achieved in the ASCPHP, facilitated by the

directional and orderly two-phase flow within its multiple channels. At an FR of 40%, the ASCPHP consistently displayed the lowest temperatures in the evaporation section across all heat loads, showcasing its superior heat transfer performance compared to conventional PHPs.

2. The ASCPHP demonstrated superior start-up performance, especially when subjected to high heat loads. It achieved thermal equilibrium most rapidly, notably at an FR of 40%, leading to a lower steady-state temperature. To be precise, the ASCPHP accomplished full start-up within a mere 1249 s at an FR of 40%, maintaining a steady temperature of around 65 °C, which marked a 12% decrease compared to the other two PHPs.
3. Adaptive structured channels significantly enhanced heat transfer efficiency and reduced the thermal resistance of the PHP, especially under high heat load conditions. When FR = 40%, the ASCPHP consistently maintained lower thermal resistance compared to the other two PHP types, achieving a maximum reduction of up to 37.5%. The lowest thermal resistance measured for the ASCPHP was 0.69 °C/W.
4. The ASCPHP effectively mitigates the adverse effects of gravity, resulting in reduced dependence on gravity for liquid replenishment and improved heat transfer performance. When placed horizontally, the ASCPHP demonstrated lower thermal resistance compared to the other two PHP types. As the orientation angle increased to 45°, the change in thermal resistance remained relatively minor, underscoring the ASCPHP's minimal reliance on gravity for its heat transfer characteristics.

In summary, the ASCPHP, as proposed, exhibits the ability to expedite start-up responses and lower thermal resistance compared to conventional PHPs. It proves particularly well-suited for high loads, leading to reduced working fluid consumption and aligning with the principles of environmentally-friendly and low-carbon development.

Author Contributions: Formal analysis, C.D. and S.W.; Funding acquisition, S.H.; Investigation, J.Y.; Methodology, S.H.; Project administration, S.H.; Resources, S.H.; Supervision, C.D. and S.W.; Validation, J.Y. and S.K.; Visualization, J.Y.; Writing—original draft, J.Y.; Writing—review and editing, S.H. All authors will be informed about each step of manuscript processing including submission, revision, revision reminder, etc. via emails from our system or assigned Assistant Editor. All authors have read and agreed to the published version of the manuscript.

Funding: This work was financially supported by the Guangdong Basic and Applied Basic Research Foundation (NO. 2023A1515010942), the Zhuhai industry university research cooperation and basic and applied basic research project (ZH22017003210001PWC), and a 2022 Suzuki foundation Scholarship and JSPS Grant-in-Aid for Scientific Research (C) Grant (NO. 20K04320).

Data Availability Statement: The details and data are currently not disclosed for public sharing. Further information can be made available upon request.

Conflicts of Interest: The authors declare no conflict of interest.

References

1. The CPC General Office. *The Chinese Government's "Guiding Opinion on the Implementation of the Digital Economy Development Plan (2021–2025)" Was Released by the General Office of the Communist Party of China (CPC)*; CPC General Office: Beijing, China, 2021.
2. The Ministry of Industry and Information Technology (MIIT). *The Ministry of Industry and Information Technology (MIIT) Has Released a Notice Titled "Plan for the Development of New-Style Data Centers (2021–2023)"*; MIIT: Beijing, China, 2021.
3. Akachi, H. Structure of a Heat Pipe. U.S. Patent 4921041, 1 May 1990.
4. Akachi, H. Structure of Micro-Heat Pipe. U.S. Patent 5219020, 15 June 1993.
5. Jang, D.S.; Lee, J.S.; Ahn, J.H.; Kim, D.; Kim, Y. Flow patterns and heat transfer characteristics of flat plate pulsating heat pipes with various asymmetric and aspect ratios of the channels. *Appl. Therm. Eng.* **2017**, *114*, 211–220. [CrossRef]
6. Wang, J.S.; Pan, Y.; Liu, X.L. Investigation on start-up and thermal performance of the single-loop pulsating heat pipe with variable diameter. *Int. J. Heat Mass Transf.* **2021**, *180*, 121811. [CrossRef]
7. Abela, M.; Mameli, M.; Nikolayev, V.; Filippeschi, S. Experimental analysis and transient numerical simulation of a large diameter pulsating heat pipe in microgravity conditions. *Int. J. Heat Mass Transf.* **2022**, *187*, 122532. [CrossRef]
8. Khandekar, S.; Schneider, M.; Schafer, P.; Kulenovic, R.; Groll, M. Thermofluid dynamic study of flat-plate closed-loop pulsating heat pipes. *Microscale Thermophys. Eng.* **2002**, *6*, 303–317. [CrossRef]

9. Yang, H.H.; Khandekar, S.; Groll, M. Performance characteristics of pulsating heat pipes as integral thermal spreaders. *Int. J. Therm. Sci.* **2009**, *48*, 815–824. [CrossRef]
10. Lee, J.; Kim, S.J. Effect of channel geometry on the operating limit of micro pulsating heat pipes. *Int. J. Heat Mass Transf.* **2017**, *107*, 204–212. [CrossRef]
11. Hua, C.; Wang, X.; Gao, X.; Zheng, H.; Han, X.; Chen, G. Experimental research on the start-up characteristics and heat transfer performance of pulsating heat pipes with rectangular channels. *Appl. Therm. Eng.* **2017**, *17*, 1058–1062. [CrossRef]
12. Miyazaki, Y. *Oscillating Heat Pipe with Check Valves, Memoirs of the Fukui Institute of Technology*; SAE: Madrid, Spain, 2002; Volume 32, pp. 389–392.
13. Rittidech, S.; Pipatpaiboon, N.; Terdtoon, P. Heat-transfer characteristics of a closed-loop oscillating heat-pipe with check valves. *Appl. Energy* **2007**, *84*, 565–577. [CrossRef]
14. Thompson, S.M.; Ma, H.B.; Wilson, C. Investigation of a flat-plate oscillating heat pipe with Tesla-type check valves. *Exp. Therm. Fluid Sci.* **2011**, *35*, 1265–1273. [CrossRef]
15. Ebrahimi, M.; Shafii, M.B.; Bijarchi, M.A. Experimental investigation of the thermal management of flat-plate closed-loop pulsating heat pipes with interconnecting channels. *Appl. Therm. Eng.* **2015**, *90*, 838–847. [CrossRef]
16. Chien, K.-H.; Lin, Y.-T.; Chen, Y.-R.; Yang, K.-S.; Wang, C.-C. A novel design of pulsating heat pipe with fewer turns applicable to all orientations. *Int. J. Heat Mass Transf.* **2012**, *55*, 2012–5722. [CrossRef]
17. Tseng, C.Y.; Yang, K.S.; Chien, K.H.; Jeng, M.S.; Wang, C.C. Investigation of the performance of pulsating heat pipe subject to uniform/alternating tube diameters. *Exp. Therm. Fluid Sci.* **2014**, *54*, 85–92. [CrossRef]
18. Kwon, G.H.; Kim, S.J. Operational characteristics of pulsating heat pipes with a dual-diameter tube. *Int. J. Heat Mass Transf.* **2014**, *75*, 184–195. [CrossRef]
19. He, Y.; Jiao, D.; Pei, G.; Hu, X.; He, L. Experimental study on a three-dimensional pulsating heat pipe with tandem tapered nozzles. *Exp. Therm. Fluid Sci.* **2020**, *119*, 110201. [CrossRef]
20. Miner, M.J.; Phelan, P.E.; Odom, B.A.; Ortiz, C.A. Experimental measurements of critical heat flux in expanding microchannel arrays. *J. Heat Transf.* **2013**, *135*, 101501. [CrossRef]
21. Miner, M.J.; Phelan, P.E.; Odom, B.A.; Ortiz, C.A. An experimental investigation of pressure drop in expanding microchannel arrays. *J. Heat Transf.* **2014**, *136*, 031502. [CrossRef]
22. Hong, S.H.; Dang, C.B.; Hihara, E.J. Experimental investigation on flow boiling in radial expanding minichannel heat sinks applied for low flow inertia condition. *Int. J. Heat Mass Transf.* **2019**, *143*, 118588. [CrossRef]
23. Hong, S.; Dang, C.; Hihara, E.; Sakamoto, H.; Wada, M. Improved two-phase flow boiling in a minichannel heat sink for thermal management of information and communication technology (ICT) equipment. *Appl. Therm. Eng.* **2020**, *181*, 115957. [CrossRef]
24. Hong, S.H.; Dang, C.B.; Hihara, E.J. Experimental investigation on flow boiling characteristics of radial expanding minichannel heat sinks applied for two-phase flow inlet. *Int. J. Heat Mass Transf.* **2020**, *151*, 119316. [CrossRef]
25. Hong, S.H.; Dang, C.B.; Hihara, E.J. A 3D inlet distributor employing copper foam for liquid replenishment and heat transfer enhancement in microchannel heat sinks. *Int. J. Heat Mass Transf.* **2020**, *157*, 119934. [CrossRef]
26. Lee, Y.-T.; Hong, S.; Chien, L.-H.; Lin, C.-J.; Yang, A.-S. Heat transfer and pressure drop of film condensation in a horizontal minitube for HFO1234yf refrigerant. *Appl. Energy* **2020**, *274*, 115183. [CrossRef]
27. Kang, Z.; Shou, D.; Fan, J. Numerical study of a novel Single-loop pulsating heat pipe with separating walls within the flow channel. *Appl. Therm. Eng.* **2021**, *196*, 117246. [CrossRef]
28. Wan, Z.; Wang, X.; Feng, C. Heat Transfer Performances of the Capillary Loop Pulsating Heat Pipes with Spring-Loaded Check Valve. *Appl. Therm. Eng.* **2019**, *167*, 114803. [CrossRef]
29. Zhan, J.R.; Chen, X.; Ji, Y.Z.; Zheng, P.; Duan, W.H. Experimental study of ethane pulsating heat pipe with varying evaporator lengths based on pulse tube refrigerator. *Int. J. Refrig.* **2023**, *145*, 40–49. [CrossRef]
30. Sagar, K.R.; Naik, H.B.; Mehta, H.B. Novel condenser based cryogenic pulsating heat Pipe: Investigations on influence of geometrical parameters. *Gryogenics* **2022**, *126*, 103543. [CrossRef]
31. Mucci, A.; Kholi, F.K.; Chetwynd-Chatwin, J.; Ha, M.Y.; Min, J.K. Numerical investigation of flow instability and heat transfer characteristics inside pulsating heat pipes with different numbers of turns. *Int. J. Heat Mass Transf.* **2021**, *169*, 120934. [CrossRef]
32. Sun, X.; Li, S.; Jiao, B.; Gan, Z.; Pfotenhauer, J.; Wang, B.; Zhao, Q.; Liu, D. Experimental study on hydrogen pulsating heat pipes under different number of turns. *Gryogenics* **2020**, *111*, 103174. [CrossRef]
33. Kim, J.; Kim, S.J. Experimental investigation on working fluid selection in a micro pulsating heat pipe. *Energy Convers.* **2020**, *205*, 112462. [CrossRef]
34. Xu, Y.; Yanqin, X.Y.; Qi, H.; Cai, W. An updated review on working fluids, operation mechanisms, and applications of pulsating heat pipes, Renew. *Sustain. Energy Rev.* **2021**, *144*, 110995.
35. Rudresha, S.; Babu, E.R.; Thejaraju, R. Experimental Investigation and Influence of Filling Ratio on Heat Transfer Performance of a Pulsating Heat Pipe. *Therm. Sci. Eng. Prog.* **2023**, *38*, 101649. [CrossRef]
36. Shi, W.X.; Chen, H.D.; Pan, L.S.; Wang, Q. Starting and running performance of a pulsating heat pipe with micro encapsulated phase change material suspension. *Appl. Therm. Eng.* **2022**, *212*, 118626. [CrossRef]
37. Ayel, V.; Araneo, L.; Scalambra, A.; Mameli, M.; Romestant, C.; Piteau, A.; Marengo, M.; Filippeschi, S.; Bertin, Y. Experimental study of a closed loop flat plate pulsating heat pipe under a varying gravity force. *Int. J. Therm. Sci.* **2015**, *96*, 2015–2023. [CrossRef]

38. Sun, Q.; Qu, J.; Wang, Q.; Yuan, J. Operational characteristics of oscillating heat pipes under micro-gravity condition. *Int. Commun. Heat Mass Transf.* **2017**, *88*, 2017–2028. [CrossRef]
39. Krambeck, L.; Domiciano, K.G.; Betancur-Arboleda, L.A.; Mantelli, M.B. Novel flat plate pulsating heat pipe with ultra sharp grooves. *Appl. Therm. Eng.* **2022**, *211*, 118509. [CrossRef]
40. Ma, H.B.; Hanlon, M.A.; Chen, C.L. An investigation of oscillating motions in a miniature pulsating heat pipe. *Microfluid. Nanofluidics* **2006**, *2*, 171–179. [CrossRef]
41. Lockhart, R.W.; Martinelli, R.C. Proposed correlation of data for isothermal two-phase, two-component flow in pipes. *Chem. Eng. Prog.* **1949**, *45*, 39–49.